

# Study of $\text{Nd}^{3+}$ , $\text{Pd}^{2+}$ , $\text{Pt}^{4+}$ , and $\text{Fe}^{3+}$ dopant effect on photoreactivity of $\text{TiO}_2$ nanoparticles

S. I. Shah<sup>\*†‡</sup>, W. Li<sup>\*</sup>, C.-P. Huang<sup>§</sup>, O. Jung<sup>¶</sup>, and C. Ni<sup>\*</sup>

Departments of <sup>\*</sup>Materials Science and Engineering, <sup>†</sup>Physics and Astronomy, and <sup>§</sup>Civil and Environmental Engineering, University of Delaware, Newark, DE 19716; and <sup>¶</sup>Department of Environmental Engineering, Chosun University, Gwang Ju, 501-759, Republic of Korea

Edited by Alexandra Navrotsky, University of California, Davis, CA, and approved January 3, 2002 (received for review October 1, 2001)

The metallorganic chemical vapor deposition method was successfully used to synthesize pure  $\text{TiO}_2$  and  $\text{Nd}^{3+}$ -,  $\text{Pd}^{2+}$ -,  $\text{Pt}^{4+}$ -, and  $\text{Fe}^{3+}$ -doped  $\text{TiO}_2$  nanoparticles. Polycrystalline  $\text{TiO}_2$  structure was verified with x-ray diffraction, which showed typical characteristic anatase reflections without any separate dopant-related peaks. Transmission electron microscopy observations confirmed the existence of homogeneously distributed  $22 \pm 3$  nm  $\text{TiO}_2$  nanoparticles. The particle size remained the same for the doped samples. The doping level of transition metals was kept at  $\approx 1$  atomic percent, which was determined by x-ray photoelectron spectra and energy dispersive x-ray spectroscopy. The effects of different types of dopants on the photocatalytic activity were revealed by the degradation of 2-chlorophenols with an UV light source. The photocatalytic efficiency was remarkably enhanced by the introduction of  $\text{Pd}^{2+}$  and  $\text{Nd}^{3+}$ .  $\text{Nd}^{3+}$ -doped  $\text{TiO}_2$  showed the largest enhancement. However,  $\text{Pt}^{4+}$  changed the 2-chlorophenol degradation rate only slightly, and  $\text{Fe}^{3+}$  was detrimental to this process. These effects were related to the position of the dopants in the nanoparticles and the difference in their ionic radii with respect to that of  $\text{Ti}^{4+}$ .

Titanium dioxide occurs in three forms (rutile, anatase, and brookite), among which anatase is believed to be the most efficient photocatalyst during chemical reactions (1, 2). It has been extensively investigated for its catalytic and electrochemical properties based on its wide applications as photocatalyst and gas sensor. Most of the studies were focused on the nanosized  $\text{TiO}_2$  with the purpose of improving the light absorption. The high surface-to-volume ratio, inherent in nanoparticles, was useful. Additionally, the small size of  $\text{TiO}_2$  crystals can make indirect band electron transition possible and increase the generation rate of electrons and holes. Increase of the generation rate of charge carriers is one way to enhance the photocatalytic activity. On the other hand, electron and hole trapping during their transportation from the interior of the particle to the surface is also very crucial to preventing the recombination of electron and hole pairs. Doping of  $\text{TiO}_2$  with transition metal ions offers a way to trap charge carriers and extend the lifetime of one or both of the charge carriers. Consequently, dopants enhance the efficiency of the photocatalyst.

The primary driving force in this research was to study the photocatalytic characteristics of  $\text{TiO}_2$  nanoparticles and the effect of transition metal dopants on  $\text{TiO}_2$  nanoparticles performance. In photocatalysis, it is the photon-generated electron-hole ( $e^-/h^+$ ) pairs that can facilitate redox reactions on particle surface. The total number of free carriers on the surface determines the efficiency of catalysts. The number and the lifetime of free  $e^-/h^+$  are particle size- and dopant-dependent. For large particles, the volume recombination of electrons and holes dominates. This condition largely reduces the number of free charges on the surface and deteriorates the photocatalytic

activity. For nanoparticles, the transportation length of  $e^-/h^+$  from crystal interface to the surface is short, which helps to accelerate the migration rate of  $e^-/h^+$  to the surface of the nanoparticle to participate the reaction process. For optimal photocatalysis efficiency there is a critical particle size below which the surface recombination of electron and hole becomes dominant because of the increased surface-to-volume ratio (3).

Besides the effect of particle size on the photocatalytic activity, the role of dopant is important. Different dopants may not have the same effect on trapping electrons and/or holes on the surface or during interface charge transfer because of the different positions of the dopant in the host lattice. Consequently, the photocatalytic efficiency would be different for different types of dopants. In this article, we describe the synthesis of  $\text{Pt}^{4+}$  nanoparticles and the effect of transition metal ion  $\text{Nd}^{3+}$ ,  $\text{Pd}^{2+}$ ,  $\text{Ti}^{4+}$ , and  $\text{Fe}^{3+}$  dopants on the photocatalytic activity of  $\text{TiO}_2$  nanoparticles. The photoactivity is investigated by performing the degradation experiments of 2-chlorophenols (2-CP). The comparison of photodegradation rates for  $\text{TiO}_2$  with and without dopants is presented.

Synthesis of  $\text{TiO}_2$  anatase nanocrystals has been achieved by several methods including impregnation (4), coprecipitation (5), sol-gel (6–8), hydrothermal method (9–11), and chemical vapor deposition (CVD) (12, 13). In our study, a metallorganic CVD (MOCVD) process was used to prepare  $\text{TiO}_2$  nanoparticles. MOCVD is preferred because it requires no postdeposition calcination, centrifugation, or hydrothermal processing to crystallize or refine particles. Also, the size distribution of particles can be simply controlled by the temperature of substrates and the flow rates of the precursors. The introduction of dopants into  $\text{TiO}_2$  nanoparticles can be realized either by a solid source, which is directly put in the proper position in the reactor, or by a solution mixed in with the liquid Ti precursor.

## Experimental Procedures

Fig. 1 shows the schematics of the MOCVD system used for the preparation of  $\text{TiO}_2$  nanoparticles. All powder samples were collected on 5-cm diameter discs made of several layers of 475-mesh stainless steel screen, which were designed to obtain high collection efficiency. Before deposition, acetone, methanol, and deionized water were used to remove any native contami-

This paper results from the Arthur M. Sackler Colloquium of the National Academy of Sciences, "Nanoscience: Underlying Physical Concepts and Phenomena," held May 18–20, 2001, at the National Academy of Sciences in Washington, DC.

This paper was submitted directly (Track II) to the PNAS office.

Abbreviations:  $e^-/h^+$ , electron-hole; 2-CP, 2-chlorophenols; CVD, chemical vapor deposition; MOCVD, metallorganic CVD; TTIP, titanium tetraisopropoxide; XPS, x-ray photoelectron spectroscopy; XRD, x-ray diffraction; TEM, transmission electron microscopy; at%, atomic percent.

<sup>†</sup>To whom reprint requests should be addressed. E-mail: ismat@udel.edu.

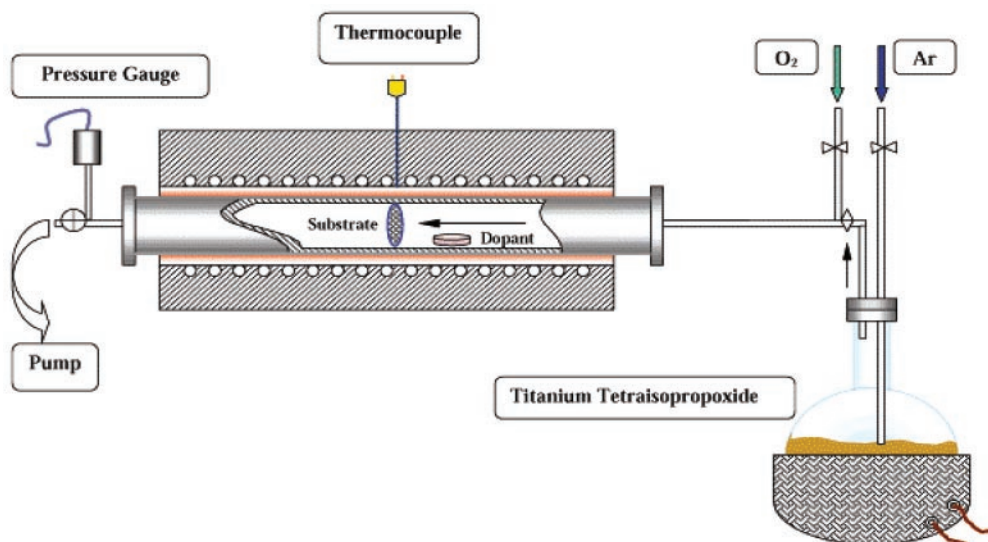


Fig. 1. Schematics of MOCVD system.

nation from the surface of the screens. The screens were held perpendicular to the flow of the reactants in the MOCVD chamber by a 3-cm diameter and 12.5-cm long quartz tube. The MOCVD chamber consisted of a 5-cm diameter and 75-cm length stainless steel tube with a central region that could be externally and uniformly heated to 1,000°C by a resistive heater. Fig. 2 shows the temperature profile of the reactor wall at 600°C. There is a 20-cm long central region and the temperature decreased toward both the ends of the reactor. The base pressure obtained by a mechanical pump was in the mTorr regime. The precursor used for Ti was  $\text{Ti}[\text{OCH}(\text{CH}_3)_2]_4$  (titanium tetraisopropoxide, TTIP, 97%). TTIP is a liquid at room temperature with a boiling point of about 232°C. TTIP was placed in a bubbling chamber that was supplied with 99.999% pure Ar as TTIP carrier gas. The temperature of the bubbling chamber and the flow rate of Ar determined the precursor flow rate, which was adjusted by changing the temperature of the bubbling chamber and/or the flow rate of the Ar through the bubbling chamber. In addition to Ar and TTIP,  $\text{O}_2$  was introduced in the MOCVD chamber to participate in the chemical reaction to form  $\text{TiO}_2$ . For the purpose of doping, neodymium (III) acetyl-

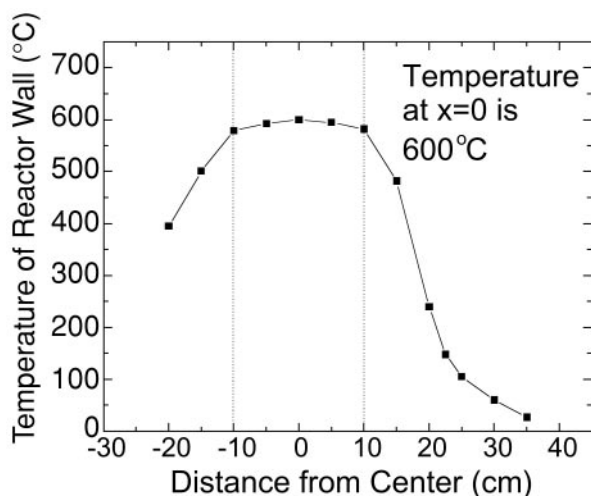


Fig. 2. Temperature profile of the reactor wall at 600°C.

acetate, palladium (II) acetylacetonate, platinum (IV) acetylacetonate, and iron (III) acetylacetonate in powder forms were used for  $\text{Nd}^{3+}$ ,  $\text{Pd}^{2+}$ ,  $\text{Pt}^{4+}$ , and  $\text{Fe}^{3+}$  ion doping, respectively. These dopant precursors were put in a Cu container, which was directly placed in the chamber. No Cu-related contamination peak was observed during the x-ray photoelectron spectroscopy (XPS) analysis. The use of Cu container does not introduce any Cu impurity because the melting point of Cu and its related oxide is much higher than the temperature at which the Cu container is used during synthesis. The incorporation rate of dopant was determined by the vapor pressure of the dopant precursor. The dopant concentration as a function of the dopant precursor temperature was measured. Thus, to obtain certain desired dopant concentration in  $\text{TiO}_2$ , dopant precursor can be placed at a predetermined position of the chamber. We used the same deposition conditions for all sample preparations in this study (see Table 1). The partial pressures of  $\text{O}_2$  and Ar were 10 Torr and 1 Torr, respectively. The temperatures for substrate and TTIP precursor were 600°C and 220°C, respectively.

X-ray diffraction (XRD) analyses were carried out for all samples. XRD  $\theta$ - $2\theta$  scans were recorded by using  $\text{Cu K}\alpha$  radiation in a Rigaku (Tokyo) D-Max B diffractometer equipped with a graphite crystal monochromator for structural characterization of the polycrystalline doped and undoped  $\text{TiO}_2$  samples. XFIT software (freeware from <http://www.ccp14.ac.uk/tutorial/xfit-95/>) was used to measure the precise  $2\theta$  positions and the full width at half maxima of the diffraction peaks. XPS and energy dispersive x-ray spectroscopy were performed for composition determination of the samples. A SSI-M Probe XPS was used with  $\text{Al K}\alpha$  exciting radiation. High-resolution scans of the Ti 2p, dopant 3d, O 1s, and C 1s regions were obtained, in addition to the survey scans, to measure the composition of the nanoparticles and to verify the valance states of Ti and the dopants. Amray (Bedford, MA) 1810T scanning electron microscopy and a JEOL 2000 FX transmission electron microscopy (TEM) were used to observe the  $\text{TiO}_2$  surface morphology and to measure the average nanoparticle size and distribution, respectively.

Photodegradation experiments were performed in the photocatalytic reactor system. This bench-scale system consisted of a cylindrical Pyrex-glass cell 20 cm in diameter and 30 cm in height with an inside reflective surface. A 100-W Hg lamp was used and immersed in the solution. A cold air-cooling jacket cooled the cell. The maximum energy emission at the wavelength of 365 nm

**Table 1. Deposition conditions, ionic radii of transition metals for a coordination number of 6(16), particle sizes obtained from XRD and TEM as well as its histogram, and photodegradation time to achieve 90% destruction of 2-CP for pure TiO<sub>2</sub> and Nd<sup>3+</sup>-, Pd<sup>2+</sup>-, Pt<sup>4+</sup>-, Fe<sup>3+</sup>-doped TiO<sub>2</sub> nanoparticles**

Sample	Pure TiO <sub>2</sub>	TiO <sub>2</sub> (Pt <sup>4+</sup> )	TiO <sub>2</sub> (Fe <sup>3+</sup> )	TiO <sub>2</sub> (Pd <sup>2+</sup> )	TiO <sub>2</sub> (Nd <sup>3+</sup> )
Substrate temperature (°C)	600	600	600	600	600
TTIP temperature (°C)	220	220	220	220	220
O <sub>2</sub> pressure (Torr)	10	10	10	10	10
Ar pressure (Torr)	1.0	1.0	1.0	1.0	1.0
Position of dopant precursor (cm)*	—	18	20	19	21.5
Dopant ionic radii (Å) <sup>†</sup>	—	0.625	0.645	0.86	0.983
Particle size from XRD (nm)	27 ± 3	28 ± 3	28 ± 3	27 ± 3	27 ± 3
Particle size from TEM (nm)	23 ± 3	23 ± 3	24 ± 2	23 ± 3	22 ± 3
Particle size from histogram (nm)	23	23	23	22	22
Time for destruction of 90% 2-CP (min)	60	50	90	40	25

\*The position refers to the distance from center of the reactor (see Fig. 2 for the temperature profile of the reactor wall at 600°C).

<sup>†</sup>Cited from ref. 16.

was achieved 4 min after the lamp was turned on. At the cooling jacket, an energy density of 5.3 mW/cm<sup>2</sup> was measured. An aqueous solution (1,000 ml) of 2-CP and the stainless steel mesh with the TiO<sub>2</sub> nanoparticles were placed in the photoreactor cell. After illumination, samples were collected at regular intervals in a test tube, and each sample solution was analyzed by HPLC (Waters model 6000 gradient system). The total organic carbon (TOC) of a sample solution was measured at constant irradiation time intervals by using a DC-190 high-temperature TOC analyzer. The Cl<sup>-</sup> ion was analyzed by ion chromatograph (Dionex) equipped with an electrochemical detector and a Dionex PAX-100 metal-free anion column (25 cm long, 4.6 mm i.d.). The eluent solution was a mixture of 80% H<sub>2</sub>O, 10% acetonitrile, and 10% 191-mM NaOH. The flow rate was 1 ml/min, and the injection loop volume was 50 μl.

The activity of the photocatalytic decomposition of 2-CP was again estimated from the yield of carbon dioxide, determined gravimetrically as BaCO<sub>3</sub>, from the yield of carbon dioxide as decreasing results of electric conductivity for Ba(OH)<sub>2</sub> solution. HCO<sub>3</sub><sup>-</sup> in a sample solution was measured by ion and liquid chromatography.

## Results

X-ray structure analysis for samples doped with different types of transition metal ions showed all of these samples had typical peaks of TiO<sub>2</sub> polycrystalline anatase nanoparticle without any

detectable dopant-related peaks. The dopants went either into the interstitial positions or substitutional sites of TiO<sub>2</sub> crystal structure. Fig. 3 shows an x-ray diffraction pattern for Nd<sup>3+</sup>-doped TiO<sub>2</sub> nanoparticles. The polycrystalline anatase structure was confirmed by (101) (004), (200), (105), and (211) diffraction peaks. Its tetragonal Bravais lattice type was also verified by lattice constant calculated from these peaks. Based on the full width at half maxima of the XRD peaks, the average particle diameter was calculated to be about 27 ± 3 nm by using Scherrer's formula. There was no measurable effect on the size of TiO<sub>2</sub> nanoparticles with the addition of different types of dopants.

XPS survey spectra for the same sample with Nd doping is shown in Fig. 4. Only peaks associated with Ti, O, and Nd were observed. The relative cation composition in the particles was determined by XPS and energy dispersive x-ray spectroscopy. The Nd concentration was measured to be about 1 atomic percent (at%). The magnified Ti 2p region is presented in Fig. 4 *Inset*. Two peaks located at 458.4 eV and 464.1 eV were identified as Ti (2p<sub>3/2</sub>) and Ti (2p<sub>1/2</sub>) (14), respectively. For metallic Ti<sup>0</sup> these two peaks are expected at 455 and 459 eV (16). The peak shifts in Ti (2p<sub>3/2</sub>) and Ti (2p<sub>1/2</sub>) peak positions and the change in the separation between these two peaks is caused by the presence of tetravalent Ti<sup>4+</sup>, which is consistent with TiO<sub>2</sub> formation (14, 15).

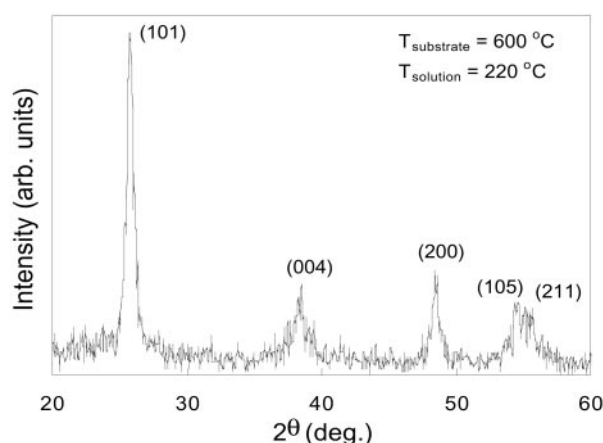


**Fig. 3.** XRD pattern of ND-doped polycrystalline TiO<sub>2</sub> nanoparticles.

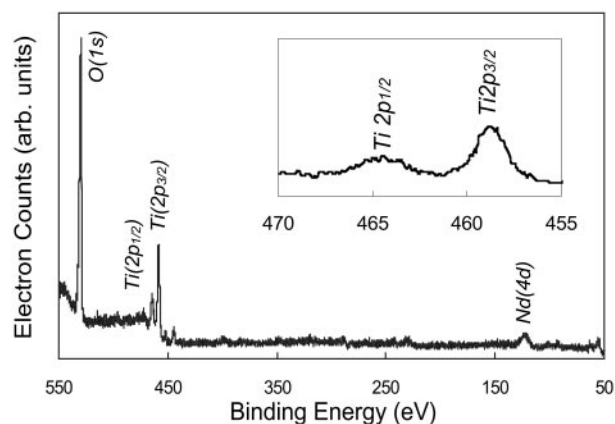


**Fig. 4.** XPS survey spectra of Nd-doped TiO<sub>2</sub> nanoparticles and the magnified Ti 2p region.

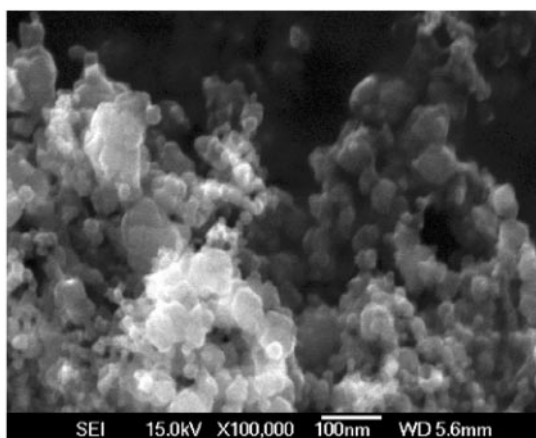


Fig. 5. Scanning electron microscopy image of TiO<sub>2</sub> nanoparticles.

Fig. 5 shows a  $\times 10,000$ -magnified scanning electron microscopy image of Nd-doped TiO<sub>2</sub> nanoparticles. The TiO<sub>2</sub> particles are aggregated together and the rough measurements from this image indicate that the size of particles is in the nanoscale range. More precise size and distribution measurements were performed by TEM. A TEM bright-field image with the diffraction pattern as an inset is shown in Fig. 6. The particle size measured was about  $22 \pm 3$  nm, consistent with the grain size measured by XRD. The electron diffraction patterns correspond to that of anatase TiO<sub>2</sub>. Fig. 7 is the histogram of particle distribution. The distribution of the size of nearly spherical particles peaked at about 22 nm with a relatively small tail toward larger values.

Fig. 8 is the comparison of the 2-CP photodegradation rates for pure TiO<sub>2</sub> sample and Nd<sup>3+</sup>-, Pd<sup>2+</sup>-, Pt<sup>4+</sup>-, and Fe<sup>3+</sup>-doped TiO<sub>2</sub> samples. In this study, the doping level in all four cases was kept constant at about 1 at%. The change of photocatalytic activity for doped samples is evident from the degradation curves. Moreover, the degradation rates for most doped samples have been enhanced with the exception of Fe<sup>3+</sup>-doped sample. The time for 90% destruction of 2-CP has been reduced from 60 min for undoped TiO<sub>2</sub> to 25 min for Nd<sup>3+</sup>-doped TiO<sub>2</sub> nanoparticles.

### Discussion

The total number of free charge carriers on the TiO<sub>2</sub> surface is determined by the rate of charge pair generation, charge trapping, charge release and migration, charge recombination as well

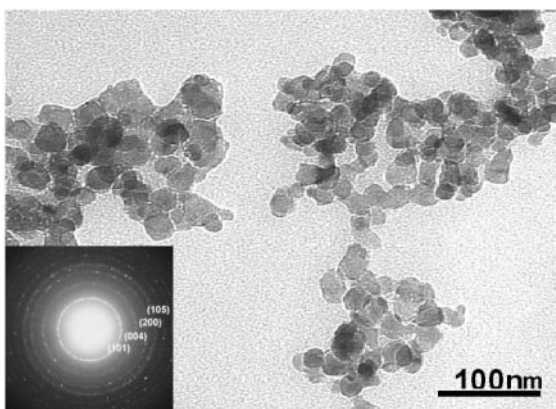


Fig. 6. TEM bright-field image of nanosized polycrystalline TiO<sub>2</sub> particles and their diffraction pattern.

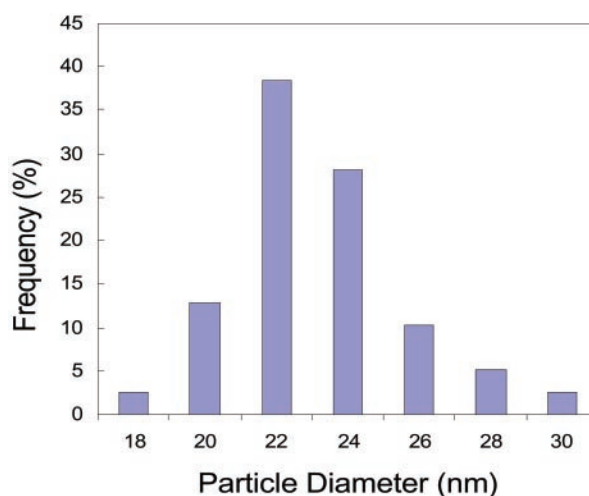
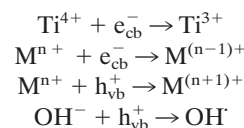


Fig. 7. Size distribution histogram of TiO<sub>2</sub> nanoparticles deposited at 600°C.

as the rate of interfacial charge transfer. The complexities of the role of transition metal ion dopants are that they can participate in all of these processes. Acting as electron and/or hole traps is the most important function of dopants. The trap of charge carriers can decrease the recombination rate of  $e^-/h^+$  pairs and consequently increase the lifetime of charge carriers. The process of charge trapping is as follows:



where  $\text{M}^{n+}$  is the metal ion dopant. The energy level of  $\text{M}^{n+}/\text{M}^{(n-1)+}$  lies below the conduction band edge and the energy level of  $\text{M}^{n+}/\text{M}^{(n+1)+}$  lies above the valence band edge. Thus, the energy level of transition metal ions affects the trapping efficiency. The trapping of electrons makes it easy for holes to transfer onto the surface of TiO<sub>2</sub> and react with  $\text{OH}^-$  in the 2-CP solution and form active  $\text{OH}^\cdot$ , hydroxyl radicals to participate the destruction of 2-CP.

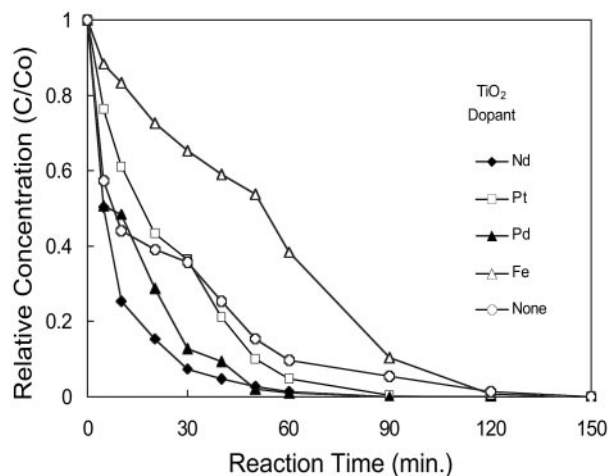


Fig. 8. Photodegradation of 2-CP with undoped TiO<sub>2</sub> and transition metal ion- (Nd<sup>3+</sup>, Pd<sup>2+</sup>, Pt<sup>4+</sup>, and Fe<sup>3+</sup>) doped TiO<sub>2</sub> under an UV light source. C<sub>0</sub> = 50 mg in 1,000 ml at pH 9.5.

2-CP degradation is an oxidation reaction for which the lifetime of the holes is critical. The lifetime of holes can be enhanced by trapping electrons, thereby reducing the recombination rate and allowing holes to diffuse to the particle surface and participate in the oxidation reaction. If the energy level of dopant ions moves toward the conduction band edge, the efficiency of trapping becomes higher. In that case, the traps have larger tendency to act as shallow traps so that the holes generated by following photons cannot recombine with the already trapped electrons. Consequently, the lifetime of free holes can be extended.

However, for transition metal ions in interstitial and substitutional positions, the change of their potential level is different and they have different trapping efficiencies for electrons. The effect of the interstitials in distorting the potential energy is larger than that of substitutional atoms. According to the XRD results of doped TiO<sub>2</sub>, only anatase phase was present in the TiO<sub>2</sub> nanoparticles and no separate dopant-related phase was observed. This finding indicates that dopant ions Nd<sup>3+</sup>, Pd<sup>2+</sup>, Pt<sup>4+</sup>, and Fe<sup>3+</sup> are either in the octahedral interstitial sites or the substitutional positions of TiO<sub>2</sub>. From the effective radii of ions for coordination number of 6 (16) in Table 1, one can see Fe<sup>3+</sup> and Pt<sup>4+</sup> have small ionic radii that are comparable to that of Ti<sup>4+</sup>, 0.605 Å. It is energetically favorable for these two ions to occupy Ti<sup>4+</sup> sites. Nd<sup>3+</sup>, on the other hand, has an ionic radius that is much larger than that of Ti<sup>4+</sup>. It is energetically favorable for Nd<sup>3+</sup> to reside in the octahedral interstitial site. The size of octahedral interstitial is large enough, 3.78 and 9.51 Å for a and c axes, respectively, to accommodate Nd<sup>3+</sup>. Pd<sup>2+</sup> also has relatively larger ionic radius and can go into the interstitial positions. Substitutionally incorporated dopants are less useful for disturbing the dopant energy level, which in turn affects the electron trapping efficiency. Pt doping shows reduced enhancement compared with Nd and Pd doping, whereas Fe doping shows lack of enhancement. There have been previous studies that show similar results for Fe on the photodegradation of the vinyl chloride (5). Another contributing reason for the lack of photocatalytic activity enhancement by Fe may include nonoptimal valency of Fe. The accurate determination of the Fe oxidation state when it is present in such low concentrations is difficult because of the problem in satisfactorily resolving the Fe 3p region of the XPS spectrum. For the interstitial dopants, the

situation is different and the potential energy level can be increased negatively toward the conduction band edge because of the oxygen affinity of dopant ions. This is the case for Nd<sup>3+</sup> and Pd<sup>2+</sup>. The high oxygen affinities of interstitially located Nd<sup>3+</sup> and Pd<sup>2+</sup> ions effectively create a localized positive charge around Ti and/or form an oxygen vacancy. The potential energy of ion dopants was disturbed and electrons were efficiently trapped. Consequently, the oxidation process of chlorophenols was remarkably improved. Currently, the doped samples had 1 at% of dopant concentrations.

TiO<sub>2</sub> nanoparticles have applications in photovoltaics, paints, etc. The enhanced performance of doped TiO<sub>2</sub> as a photocatalyst suggests that its performance for other applications also may be improved. However, these particles have to be analyzed specifically for the pertinent application.

## Conclusions

Crystalline doped and undoped TiO<sub>2</sub> anatase nanoparticles (22 ± 3 nm) were successfully synthesized by using MOCVD at 600°C substrate temperature and 220°C precursor solution temperature. The effect of the different type dopants, Nd<sup>3+</sup>, Pd<sup>2+</sup>, Pt<sup>4+</sup>, and Fe<sup>3+</sup>, with similar concentration (≈1 at%) on the photocatalytic efficiency was investigated by performing the photodegradation of 2-CP under radiation of UV light. Results showed that the efficiency of photocatalyst was remarkably enhanced for Nd<sup>3+</sup>- and Pd<sup>2+</sup>-doped TiO<sub>2</sub>. In particular, the 90% destruction time of 2-CP was reduced from 60 min for the undoped TiO<sub>2</sub> nanoparticles to 25 min for the 1 at% Nd-doped nano TiO<sub>2</sub>. On the other hand, Pt<sup>4+</sup> caused only a slight decrease in the 2-CP oxidation time and Fe<sup>3+</sup> did not help at all. Possible explanations could be based on the change of potential energy level for different positions of dopants in TiO<sub>2</sub> lattice. The position of dopants is determined by the size differences between the host Ti<sup>4+</sup> ionic radius and the dopant's ionic radii. Nd<sup>3+</sup> and Pd<sup>2+</sup> acted as interstitial dopants. Large disturbance of the potential energy resulted in the creation of localized positive charge around Ti and/or formation an oxygen vacancy, which consequently enhanced the electron trapping efficiency. However, Pt<sup>4+</sup> and Fe<sup>3+</sup> were presumably in substitutional positions with very little or no potential energy disturbance. They were less useful for the electron trapping. More experiments, including near edge x-ray absorption fine structure and XPS, are necessary to locate the position of dopants in TiO<sub>2</sub> lattice.

1. Sclafani, A., Palmisano, L. & Davi, E. (1991) *J. Photochem. Photobiol. A* **56**, 113–123.
2. Vidal, A., Herrero, J., Romero, M., Sanchez, B. & Sanchez, M. (1994) *J. Photochem. Photobiol. A* **79**, 213–219.
3. Beydoun, D., Amal, R., Low, G. & McEvoy, S. (1999) *J. Nanoparticle Res.* **1**, 439–458.
4. Litter, M. I. & Navio, J. A. (1994) *J. Photochem. Photobiol. A* **84**, 183–193.
5. Palmisano, L., Augugliaro, V., Sclafani, A. & Schiavello, M. (1988) *J. Phys. Chem.* **92**, 6710–6713.
6. Choi, W., Termin, A. & Hoffmann, M. R. (1994) *J. Phys. Chem.* **98**, 13669–13679.
7. Zhang, Z., Wang, C.-C., Zakaria, R. & Ying, J. Y. (1998) *J. Phys. Chem. B* **102**, 10871–10878.
8. Wang, C.-C., Zhang, Z. & Ying, J. Y. (1997) *NanoStructured Mater.* **9**, 583–586.
9. Wang, Y., Cheng, H., Hao, Y., Ma, J., Li, W. & Cai, S. (1999) *J. Mater. Sci.* **34**, 3721–3729.
10. Cheng, H., Ma, J., Zhao, Z. & Qi, L. (1995) *Chem. Mater.* **7**, 663–671.
11. Wang, Y., Hao, Y., Cheng, H., Ma, J., Xu, B., Li, W. & Cai, S. (1999) *J. Mater. Sci.* **34**, 2773–2779.
12. Ding, Z., Hu, X., Lu, G. Q., Yue, P.-L. & Greenfield, P. F. (2000) *Langmuir* **16**, 6216–6222.
13. Schrijnemakers, K., Impens, N. R. E. N. & Vansant, E. F. (1999) *Langmuir* **15**, 5807–5813.
14. Wagner, C. D., Riggs, W. M., Davis, L. E., Moulder, J. F. & Muilenberg, G. E., eds. (1979) *Handbook of X-Ray Photoelectron Spectroscopy* (Perkin-Elmer, Eden Prairie, MN).
15. Sen, S. K., Riga, J. & Verbist, J. (1976) *Chem. Phys. Lett.* **39**, 560–564.
16. Shannon, R. D. (1976) *Acta Crystallogr. A* **32**, 751–767.